A hybrid numerical and machine learning framework for evaluating the performance of a 780 cm^2 aqueous organic redox flow battery

Yunxiang Chen[a,*], Chao Zeng[a], Yucheng Fu[a], Jie Bao[b], Peiyuan Gao[a], Justin Chen[b], Zhijie Xu[a], Soowhan Kim[b], Aaron Hollas[b], Wei Wang[b]

[a]*Physical and Computational Sciences Directorate, Pacific Northwest National Laboratory, Richland, Washington, USA 99354.*
[b]*Energy and Environment Directorate, Pacific Northwest National Laboratory, Richland, Washington, USA 99354.*

Abstract

Aqueous organic redox flow battery (AORFB) is a promising cost-competitive technology for large-scale energy storage. Among AORFBs, the dihydroxyphenazine (DHP)-based AORFB has demonstrated high energy density and low-capacity degradation in small-scale lab tests. However, its commercial scale performance remains unknown. This work comprehensively evaluates the performance of a 780 cm^2 DHP-based AORFB by combining a physics-based numerical model, machine learning (ML)-based surrogate models, and ML-derived sensitivity quantification. Specifically, we first select 12 battery parameters that include 10 physicochemical and 2 operation quantities. 12800 combinations of these parameters are subsequently generated using the Latin Hypercube Sampling. Together with 38 pre-defined State of Charge, such combinations are integrated into a validated AORFB model developed in COMSOL to compute 6 performance metrics. The parameters and perfor-

*Corresponding author: Yunxiang Chen, yunxiang.chen@pnnl.gov

mance data are then used to train 60 deep neural network (DNN) surrogate models for further sensitivity score calculation. Two additional sensitivity analysis tools (MARS and SHAP) are also used to cross-validate the sensitivity scores from the DNN. The results demonstrate that 1) standard potential ranks first in controlling energy efficiency (EE) and charging energy, 2) membrane conductivity is most critical for power loss and EE, and 3) specific area and reaction rate control activation power loss.

Highlights

- A hybrid numerical-ML framework is proposed for large-scale AORFB performance study
- Over 400,000 cell voltage and 10,000 battery performance data are generated
- The sensitivity of 6 cell performance metrics to 12 parameters is studied
- Standard potential ranks as top 2 control of energy efficiency and charging energy
- Membrane conductivity ranks as top 2 control of power loss and energy efficiency

Keywords: Aqueous organic redox flow battery, battery performance, operation conditions, physicochemical parameters, machine learning

---

1. Introduction

Vanadium redox flow battery (RFB) is one of the most mature grid-scale and long-duration energy storage solutions for intermittent wind and solar energies [6, 8, 9, 37, 45]. High cost of vanadium, however, is a cost-barrier for its

large-scale deployment [9, 31]. Aqueous Organic RFB (AORFB), which uses organic active materials in one or both sides of the cell, is a cost-competitive solution because active organic species can be synthesized from low-cost and abundant materials [10, 17, 25, 26]. One of such materials is the dihydroxyphenazine (DHP)-based organic materials family, which has demonstrated a reversible capacity of 67 Ah/L and 0.02% capacity degradation rate per cycle over 500 cycles [17]. However, such performance is achieved in idealized lab environments using a small (i.e., 10 cm^2) cell [17]. It is not clear how such performance will respond to the flow and active species concentration heterogeneity in large cell and the diverse conditions of real-world environments, which poses a barrier for its commercial-scale demonstration and deployment.

From previous research on inorganic and organic RFBs, it is found that the diverse environments can affect battery performance by modulating key parameters of the cell microstructure, electrolyte physicochemical properties, membrane properties, and operating conditions [3, 4, 17, 45]. The cell size can also affect cell performance by regulating the heterogeneity in flow and active species concentration distributions [13, 43]. To gain a comprehensive understanding of the effects of cell size and environment-modulating parameters, a cell size much larger than the typical lab-scale is firstly needed. Additionally, an approach that can quantify the cell voltage and performance using various cell microstructure, electrolyte physicochemical properties, and membrane properties under various flow rate and current density conditions is needed. The first requisite is achievable by using a 780 cm^2 interdigitated cell developed by PNNL team [30]. The second requisite can be generally

achieved using either experiments or numerical modeling or their both. However, considering the high costs in labor, time, and materials preparation, large-scale AORFB experiments can only be performed a few times and used as validation data for physics-based numerical models. The validated numerical model is best suitable for generating the cell voltage and performance data by changing the key parameters of the numerical model. A previous work by Zeng et al. [43] demonstrated the feasibility of using COMSOL Multiphysics® to simulate the potentials and performance of a 780 cm^2 cell with a DHP-family material and ferro/ferricyanide as working electrolytes. Such a model provides the basis to generate cell performance data. However, this model takes about 128 CPU hours to simulate one charge-discharge cycle with around 38 SoC points, which is time- and computing-prohibitive for a comprehensive sensitivity study because we need to vary 12 independent parameters for each charge-discharge cycle.

To reduce the computational costs, further assumptions or steps are needed. The first assumption is to assume the physicochemical parameters of the positive electrode and electrolyte are constant because the ferro/ferricyanide catholyte is much more well-known than the organic anolyte. With this assumption, this work only considers the effects of the parameters in negative cell as listed in Table 1. Second, we used the Latin hypercube sampling (LHS) method to generate 1280 samples for 10 parameters at each given flow rate and current density, which could generate near random and uniform samples of the key parameters. With such sampling parameters and the fixed parameters in positive cell, around 1000 validate cell voltage and performance data can be generated from the COMSOL model in step 3. With the sampled

parameters and COMSOL-generated performance data, we trained machine learning (ML)-based surrogate models to represent the relationship between the battery performance and input parameters at each given flow rate and current density using three approaches: a newly developed DNN model, the Multivariate Adaptive Regression Splines (MARS) model, and the SHapley Additive exPlanations (SHAP) model. These models can be used to quantify the relative importance of each input parameter in the targeting cell performance metrics and identify the dominant factors controlling cell performance. It is worth mentioning that the DNN is selected because the data sets used for surrogate model training are non-distributed and non-sequential. Such data sets are not preferred for use with Convolutional Neural Networks or Recurrent Neural Networks models that work best with spatial and sequential data, respectively[18]. The SHAP is selected due to more rigorous theoretical basis, better global interpretability, and wider applications than the Local Interpretable Model-agnostic Explanations (LIME) approach [27].

Following these steps, the paper is organized as follows. Section 2 introduces the hybrid numerical-ML framework as well as the details of parameter selection, sampling, cell performance generation using COMSOL, performance data processing and subsequent sensitivity quantification using DNN, MARS, and SHAP. Section 3 introduces the details of experiment setups for COMSOL validation. Section 4 reports the results of COMSOL model validation, DNN training accuracy, and the dominant factors that control the cell performance, as well as multi-model comparison for sensitivity score quantification. The final discovery is summarized in Section 5.

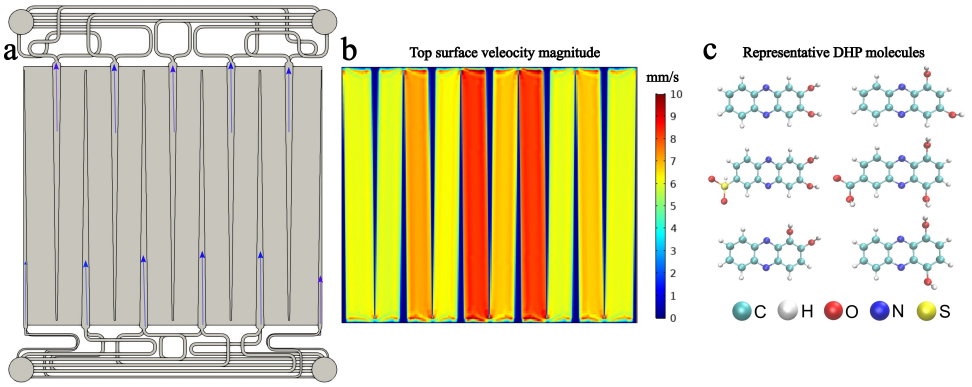

Figure 1: The geometric structure of a 780 cm^2 cell developed at PNNL (a), its heterogeneous flow field (b), as well as representative molecule structures of the DHP family (c). Blue arrows in (a) represent the direction of flow.

2. Methods

2.1. Framework

The sensitivity study is conducted using a hybrid numerical and machine learning model framework as shown in Figure 2. With it, we first select 12 influential parameters on battery performance, including 10 physicochemical parameters and 2 operation parameters (a), then generate 486,400 samples of the combinations of physicochemical parameters, state of charge (SoC), and operation parameters (b). These parameters are sent to a 780 cm^2 AORFB numerical model, which is developed in COMSOL, a finite element software, to obtain the cell voltage and its potential components for each sample parameter (c). The numerical model yields 306,140 valid results, from which, 10,300 valid cell cycle performance data are computed (d). Such numerical model-derived performance data (of the size 10300 $\times$ 6) are then combined with the corresponding parameters (of the size 10300 $\times$ 12) to

train 60 deep neural network (DNN) models. These 60 DNNs represent surrogate models between the 6 performance metrics and the physicochemical parameters at a given flow rate (5 values) and current density (2 values). These DNN models are then used to quantify the sensitivity score of the input parameters to the performance metrics. The details of each step are introduced in the following sections.

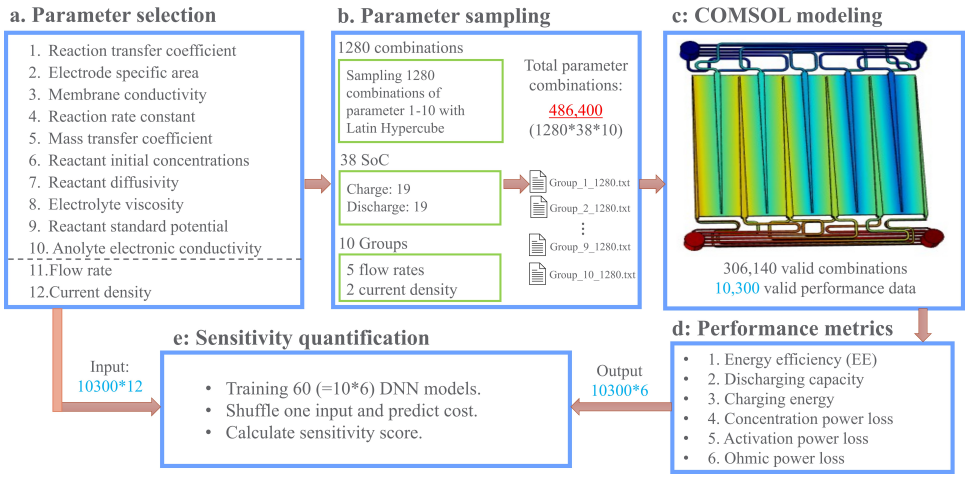

Figure 2: A hybrid numerical and deep neural network (DNN) framework for redox flow battery performance sensitivity analyses.

2.2. Parameters selection and sampling

Based on our previous work [3–5, 43, 44], we selected 10 physicochemical parameters and 2 operation parameters as key factors that can potentially impact the battery performance. The physicochemical parameters include the specific area of the negative electrode, membrane ionic conductivity, mass transfer coefficient; the reaction transfer coefficient, reaction rate constant, and standard potential of the DHP redox couple; as well as the diffusivity,

viscosity, ionic conductivity, and initial concentration of DHP anolyte. The operation parameters include pump flow rate and current density. Temperature is another typical operation parameter, however, its impact on battery performance is not explicitly considered in this work because all the experiments for the 780 cm^2 cell are conducted in a controlled laboratory environment. Nevertheless, the temperature effect can be inferred indirectly through the random sampling of the physicochemical parameters that vary with temperature. The range of operation parameters are 0.4, 0.8, 1.2, 1.6, and 2.0 L/min for pump rate and 1600 and 2400 A/m^2 for current density, both of which are determined from experiment setups. The range of physicochemical parameters is derived based on a baseline case for 7,8-dihydroxyphenazine-2-sulfonic acid (DHPS), which has measured parameters [17]. We set $\pm 50\%$ of the baseline values as the sample range of these parameters. The details of the sample range can be found in Table 1. Different from the rest parameters, the range of the standard potential, in relation to the Standard Hydrogen Electrode (SHE), of the DHP-family materials are derived from both previous experiment database [1, 2, 7, 15, 16, 19–24, 28, 32–36, 38–42] and our newly developed graph-based Gaussian processing regression algorithm [14]. Our new algorithm is trained from existing database and can predict the redox potential of organic molecules such as quinones and phenazines with various functional groups at different positions.

After we determine the range of these parameters, we use the Latin hypercube sampling (LHS) approach to generate 1280 samples for each given flow rate and current density. Because battery voltage varies with SoC, we selected 38 SoC with 19 for discharge and 19 for discharge. The range of SoC

is between 0.025 and 0.85 to represent a typical range. In total, we generated 486,400 (= 1280×38×5×2) parameter combinations for physicochemical parameters (1280), SoC (38), flow rate (5), and current density (2). These parameters are only used for the anode. For the cathode, the parameters are determined from experiments and kept unchanged for all simulations. A full list of the parameters used for cathode can be found in Supplementary Information. After generating these parameters, they are sent to COMSOL to solve the coupled flow and reactive transport equations to obtain cell voltage and its contributing components such as equilibrium, concentration, activation, ohmic potentials in both cathode and anode as we as the membrane ohmic potential. The details of the COMSOL model are introduced in Section 2.3.

Table 1: Sensitivity parameters and their range.

ID	Name	Unit	Baseline	Min	Max	Mean
1	Reaction transfer coefficient	1	0.50	0.30	0.70	0.50
2	Electrode specific area	1/m	5.9e4	1.2e4	1.2e5	6.5e4
3	Membrane conductivity	S/m	0.833	0.5	2.0	1.25
4	Reaction rate constant	m/s	1.47e-4	1.0e-8	1.5e-3	5.9e-4
5	Mass transfer coefficient	1	1	0.5	50	25.25
6	Initial concentration	mol/m3	1000	50	1500	775
7	Reactant diffusivity	m^2/s	4.81e-10	4.88e-11	4.81e-9	2.43e-9
8	Electrolyte viscosity	Pa.s	3.4e-3	1.0e-3	1.2e-2	6.5e-3
9	Reactant standard potential	V	NA	-1.4	-0.1	-0.75
10	Anolyte conductivity	S/m	10	10	100	55
11	Pump flow rate	L/min	NA	0.4	2	1.2
12	Current density	A/m^2	NA	1600	2400	2000

2.3. Cell geometry and COMSOL modeling

Prototype stack development has been taken in PNNL for over 10 years. The basic unit of this up-to-date stack is the 780 cm^2 interdigitated cell. The

much higher energy efficiency has been achieved for this interdigitated design as comparison to conventional flow-through design [29]. This unit interdigitated cell with active area of 780 cm^2 is employed as model geometry in this study (Figure 1a). This cell has width of 0.3 m (Figure 1b horizontal dimension) and length of 0.26 m (Figure 1b) vertical dimension). There are six inlet flow channels and five outlet channels. The manifold is used to distribute the electrolyte uniformly into each inlet channel. The electrode thickness is 0.64 mm and the membrane thickness is 50.8 μm. The fabrication and testing demonstration of this cell for vanadium has been presented in reference [29]. In this study, the PNNL-developed alkaline organic anolyte DHPS is modeled following the same setting as our prior work [43]. In brief introduction, four coupled physics has been considered in the model: the transport of electroactive species, electrochemical reaction kinetics, electrical field, and flow field. It is noted that there are two electrons transferred for DHPS electrolyte and only one electron transferred for ferro/ferricyanide electrolyte. Therefore, the reaction kinetics, described by the extended Bulter-Volmer equation, present different form. In addition, the governing equations in flow channel manifold are different than those in porous electrode, due to the lack of electrochemical reaction. The detailed governing equations of the model and mesh setups can be found in our prior work [43]. The simulation is conducted in COMSOL Multiphysics software. Stationary solver is used to simulate situation at different SoC condition. The flow field is solved first since it is independent with other physics. Then, species transport, reaction kinetics and electrical field are solved by fully coupled solver.

To facilitate automated feeding of the sampling parameters to the COM-

SOL, two Matlab scripts were developed to write anode sampling parameters (10 physicochemical parameters and 2 operation conditions) and SoC values to formats readable by COMSOL. The outputs from COMSOL for each case were also converted to a standard csv format using a Matlab script for further model validation, data processing, and ML. Due to the non-uniformity in velocity and local current density, the COMSOL outputs the cell voltage (E_c) and the power attributed to equilibrium (P_{eq}), activation (P_{act}), ohmic (P_{ohm}), and concentration (P_{con}) for both electrodes as computed by Equations 1 – 4. Here the E_{eq}, E_{act}, η_{ohm}, and E_{con} denote the spatially varying equilibrium, activation, ohmic, and concentration potentials. The i and a is the local current density and specific area. And dV is the volume of a single mesh. The calculated power is a function of SoC and also a function of time (t). The conversion of SoC to time is achieved through Equations 5 – 6 with t^c and t^d representing charge time and discharge time. Other symbols denote starting SoC in charge (SoC_s^c), number of electrons in anode (n), Faraday constant (F), anode tank volume (V_t), total concentration in anode (C_N), and current (I_t), ending SoC in charge (SoC_e^c), and the ending time of charge (t_c^e).

$$P_{eq} = \int_V E_{eq} \cdot i \cdot a \cdot dV = P_{eq}(SoC) = P_{eq}(t) \tag{1}$$

$$P_{act} = \int_V E_{act} \cdot i \cdot a \cdot dV = P_{act}(t) \tag{2}$$

$$P_{ohm} = \int_V \eta_{ohm} \cdot i \cdot a \cdot dV \tag{3}$$

$$P_{con} = \int_V E_{con} \cdot i \cdot a \cdot dV = P_{con}(t) \tag{4}$$

$$t^c = (SoC - SoC_s^c) \cdot nFV_tC_N/I_t \tag{5}$$

$$t^d = (SoC_e^c - SoC) \cdot nFV_tC_N/I_t + t_e^c \tag{6}$$

2.4. Data cleaning and processing

The COMSOL modeling provides 10 variables (i.e., cell voltage, equilibrium, activation, concentration, ohmic power in positive and negative, as well as membrane ohmic power) that vary with SoC (or time). To make sure the simulated data have a representation of the varying SoC, we only keep the cases that have at least 5 data points in both charging and discharging. This results in 306,140 valid points out of 486,400 sampling points and 10,300 valid voltage curves out of 12,800 sampling curves, which means the ratio of valid points and curves are around 62.9% and 80.5%, respectively. From these data, we compute the battery performance via 6 metrics, including energy efficiency (EE), discharging capacity, charging energy, concentration power loss, activation power loss, and ohmic power loss. These metrics are calculated by Equations 7 – 12. It is worthy noting that the Coulombic efficiency is set to 1, and therefore, the time during discharging equals the time of charging.

$$EE = \int_{t_s^d}^{t_e^d} E_c \cdot I_t \cdot dt / \int_0^{t_c^e} E_c \cdot I_t \cdot dt \tag{7}$$

$$c_d = (t_e^d - t_s^d) \cdot I_t \tag{8}$$

$$e_c = \int_0^{t_c^e} E_c \cdot I_t \cdot dt \tag{9}$$

$$p_{con} = (\int_0^{t_c^e} P_{con} \cdot I_t \cdot dt + \int_{t_s^d}^{t_s^e} P_{con} \cdot I_t \cdot dt)/(t_e^d - t_s^d) \tag{10}$$

$$p_{act} = (\int_0^{t_c^e} P_{act} \cdot I_t \cdot dt + \int_{t_s^d}^{t_s^e} P_{act} \cdot I_t \cdot dt)/(t_e^d - t_s^d) \tag{11}$$

$$p_{ohm} = (\int_0^{t_c^e} P_{ohm} \cdot I_t \cdot dt + \int_{t_s^d}^{t_s^e} P_{ohm} \cdot I_t \cdot dt)/(t_e^d - t_s^d) \tag{12}$$

2.5. DNN model and sensitivity score

Based on the data processing approach, we generated a battery performance database of the size 10,300 rows and 19 columns. The 19 columns including 12 sampling parameters, 6 battery performance metrics, and battery charging time. In the sampling parameters, we have 5 flow rates and 2 current densities. We split the whole datasets into 10 groups with each group represents a single flow rate and current density. If denoting the dataset for each group by X and their row and column number by nr and nc, then $nc = 19$ and nr has minimum, mean, and maximum values of 765, 1130, and 1120, respectively. For each dataset X, we trained 6 DNN models. The input of these DNN models are the 10 sampling parameters, and output is one of the 6 battery performance metrics. If denoting the inputs by $\vec{x} = [x_1, x_i, ..., x_{10}]$ and output by y^j, then each trained DNN represents a surrogate physical model in the format of $y^j = DNN^j(\vec{x}; I, Q)$ with I and Q representing the given current density and flow rate.

The DNN weighs are obtained through training using Tensorflow. The ratio of data used for training, validation, and testing is 80.75%, 4.25%, and 15%, respectively. The training target is to minimize the average squared error between the training data (i.e., battery performance data) and the DNN-predicted values using the Adam optimizer. Other important parameters for the DNN include DNN size of 256×512×256, learning rate 1e-4, and

batch size 8. During the training, we recorded the minimum cost at each step (Figure 4a blue line), and compare any new cost (Figure 4a purple square) with the recorded minimum cost in each step. The final DNN is the model that reaches the minimum cost for the first time and stays unchanged for 1500 new training steps. The convergence history of the costs during the training is illustrated in Figure 4.

With the trained surrogate model, we compute the sensitivity of a specific sample parameter (x_i) to the target (y_j) using input parameter random shuffle method. Specifically, we first compute the testing cost (denoted by $Cost_i^{j,0}$) using the testing input parameters $\vec{x} = [x_1, x_i, ..., x_{10}]$; then we replace such input parameter by $\vec{x}^S = [x_1, x_i^S, ..., x_{10}]$ with x_i^S representing the randomized values of x_i; then we calculate the cost of the shuffled inputs (denoted by $Cost_i^{j,S}$); and finally compute their difference as $Cost_i^{j,S} - Cost_i^{j,0}$. Such a cost difference is used to quantify how sensitive of the target battery performance (via surrogate model DNN^j) to the specific input parameter (x_i). By applying this procedure to all the 10 input parameters, the relative sensitivity of each parameter can be calculated by Equation 13.

$$SC_i^j(I,Q) = \frac{Cost_i^{j,S}(I,Q) - Cost_i^{j,0}(I,Q)}{\sum_1^{10}\left[Cost_i^{j,S}(I,Q) - Cost_i^{j,0}(I,Q)\right]} \tag{13}$$

2.6. MARS

To evaluate whether the DNN model causes systematic bias, we also analyzed the importance of those 12 parameters with the MARS method. The MARS technique is a nonlinear regression model commonly used for data regression and sensitivity analysis. This method, proposed by Friedman in

1991, extends the capabilities of traditional recursive partitioning regression models, providing a more versatile framework for analyzing complex data sets [11, 12]. At the core of the MARS approach is the surrogate model, $\hat{f}_M$, which is expressed as a sum of a set of basis functions:

$$\hat{f}_M(x) = \sum_{i=1}^{M} c_i B_i(x) \tag{14}$$

Each basis function $B_i(x)$ can be a constant, a hinge function, or a product of two or more hinge functions. This structure allows the model to capture both piecewise linear relationships and complex interactions between variables. The flexibility of the MARS method enables users to customize the model complexity by selecting an appropriate number and type of hinge functions. The coefficients c_i represent the weights of the basis function $B_i(x)$, are determined by minimizing the residual sum of squares (RSS), defined as Equation 15.

$$\text{RSS} = \sum_{i=1}^{n} (y_i - \hat{f}(x_i))^2 \tag{15}$$

This process involves adjusting the coefficients to minimize the observed and predicted values, thereby improving model predictive accuracy.

The selection of basis functions is conducted in two stages: forward selection and backward elimination. During forward selection, basis functions are added sequentially, with each new function chosen based on its ability to reduce the training error the most. This process continues until the number of basis functions reaches a predefined maximum. To address potential overfitting from forward selection, backward elimination is performed. In this step, the generalized cross-validation (GCV) score is used as the elimination

criterion, calculated as Equation 16.

$$GCV = \frac{\frac{1}{N}\sum_{i=1}^{N}\left(y_i - \hat{f}_M(x_i)\right)^2}{\left(1 - \frac{C(M)}{N}\right)^2} \tag{16}$$

The numerator represents the mean RSS of the MARS model and the N here stand for the total number of observations in the simulations. The term $C(M)$ represents the effective number of parameters, which penalizes the addition of excessive basis functions.

To assess the influence of each input parameter on the AORFB performance metrics, the sensitivity score is derived using the GCV scores. For each input parameter, the basis functions involving that parameter are removed from the trained model $\hat{f}M(x)$. A new GCV score is then calculated for the model without that input parameter. The sensitivity score for each parameter is determined by subtracting the full-model GCV from the GCV of the reduced model:

$$s_i = \mathrm{GCV}(M_{x_i}) - \mathrm{GCV}(M) \tag{17}$$

A higher sensitivity score s_i indicates a significant increase in model error when the corresponding parameter is excluded, suggesting that this input parameter has a greater impact on the output compared to others.

2.7. SHAP

The SHAP library has emerged as a potentially pivotal instrument in the field of machine learning model interpretation and explainability. As machine learning models grow in complexity and find applications in various

domains, understanding the rationales behind their predictions becomes increasingly crucial. SHAP offers a comprehensive framework for attributing the contribution of individual features to predictions, granting insight into the "black-box" nature of intricate models. SHAP values are rooted in Shapley values from cooperative game theory, a concept that assigns a value to each player in a coalition based on their contribution to the total outcome. SHAP values aim to provide local explanations for individual predictions. For a specific instance, SHAP values quantify the impact of each feature on the prediction compared to a baseline or average prediction. This feature importance provides an explanation as to why a particular prediction was made by identifying which features had the most influence. SHAP values adhere to certain axioms like consistency and fairness, which makes them reliable for interpretation across different models and use cases. They offer a consistent way of attributing feature importance, enabling meaningful comparisons between different predictions and models.

In this study, the 60 trained DNN models as introduced in Section 2.5 were loaded into SHAP explanation model. A SHAP value is calculated for each input value, resulting in 12 SHAP values for each output. Positive SHAP values indicate features that push the output prediction higher, while negative values indicate features that pull the prediction lower. The total range that an input parameter (physicochemical properties and operation conditions) can adjust on the output parameter is used as the overall importance score of this input parameter on the selected output parameter.

3. Experiments

To confirm the accuracy of the developed numerical model, experimental data have been collected for validation purposes. An interdigitated flow cell is assembled by sandwiching a Nafion membrane (N212) between carbon electrodes, where the carbon electrode consists of two carbon clothes (Elat H) for anode and cathode each. The carbon cloth is selected due to demonstrated higher power capability, lower pressure drop, and shorter flow path in the cell when it is paired with our advanced interdigitated stack design. The porous electrodes are heated-treated in air at 400 °C for 6 hours prior to use. The electrode is embedded into the cavity (0.3 m $\times$ 0.56 m $\times$ 0.64 mm in width, length, and thickness) of bipolar plates with a compression ratio of around 20%. The active cross-sectional area is 780 cm^2.

To prepare the electrolyte, $VOSO_4 \cdot xH_2O$ (where x is experimentally determined as 4.33) is dissolved in mixed acid (hydrochloric and sulfuric acid). The acquired electrolyte is a solution of 2 M Vanadium in 2 M H_2SO_4 and 5 M HCl. The addition of chloride ions not only increases the concentration but also reduces the viscosity of the electrolyte. Two reservoir tanks each with 2 L of electrolyte were used for both the anode and cathode sides. The room temperature is controlled at 25 °C. In full cell cycling, the cut-off voltage for charging is 1.75 V and 1.0 V for discharging. After completing one cycling test, several minutes of cool-down period is applied to reduce the effect of rising temperature prior to the next cycling test. It is worth mentioning that such experiments are conducted only for the vanadium flow battery to study how the heterogeneity in flow and species concentrations caused by larger cell size affects the overall battery performance. Such an approach, i.e., us-

ing vanadium in large stack cell, is also used by a commercial company to validate the performance of its organic chemicals due to similar viscosity and flow distributions between the two materials. In this work, large-cell organic flow battery experiments have not been completed due to the high demand of the organic materials. The PNNL stack test bench consists of 3-gallon (11.36 L) tanks and centrifugal chemical pumps. The minimum amount of DHPS required to run the test bench is 0.6 kg which is a huge amount in lab-scale test because DHPS is not commercially available now. However, experiments on small cell AORFB using DHPS have been reported in our previous work [43].

4. Results and discussion

4.1. Model validation for COMSOL

Because the DNN, MARS, and SHAP need the COMSOL data as training and testing data, it is critical to evaluate the accuracy of the 780 cm^2 AORFB model in reproducing cell voltages. Figure 3 compares the voltage data from COMSOL and experiment over typical SoC ranges with 3 flow rates used in the large call vanadium RFB experiments. The result demonstrates that COMSOL can well reproduce the experiment data. By interpolating the experiment data to the same SoC used in COMSOL, the root mean square between the two data during charging is 9.38, 18.49, and 19.39 mV for flow rate at 0.39, 0.78, and 1.17 L/min, respectively. Those during discharging are 10.63, 20.77, and 16.46 mV, respectively. The maximum absolute relative errors between the two data during charging are 1.22%, 2.55%, and 2.36% and those during discharging are 1.18%, 3.92%, and 2.97%, respectively. These

results confirm the quantitative accuracy of the COMSOL model in reproducing the cell voltage in a large cell using vanadium electrolyte. Though experiment data of large-cell organic RFB are not available, our previous work demonstrated that the cell voltage can be well reproduced for small-cell organic RFB [43]. These results suggest the validated large-scale RFB model for vanadium is likely applicable to large-scale organic RFB modeling.

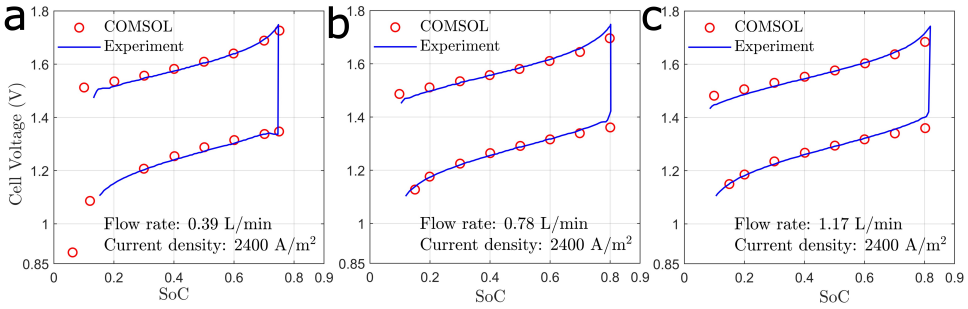

Figure 3: The comparison of cell voltage between COMSOL and experiments at pump rate 0.39 (a), 0.78 (b), and 1.17 (c) L/min with identical current density 2400 A/m^2. The experiments are performed for 780 cm^2 vanadium RFB.

4.2. DNN training accuracy

As mentioned in Section 2.5, we trained 60 DNN models with each representing a combination of one flow rate (total 5), one current density (total 2), and one performance metric (total 6). Figure 4a shows the evolution of the training and validation costs with respect to the training step for energy efficiency. The result suggests the training cost can decrease to a much smaller value, however, the validation cost will not improve after a certain step. The final model is determined as the model whose validation cost is minimum and shows no improvement for 1500 steps. Such selection can

guarantee sufficient training but without overfitting. The comparison of the well-trained DNN prediction with the COMSOL for training (Figure 4b) and testing (Figure 4c) suggest sufficient and accurate training. The 1:1 comparisons and their quantitative error metrics, i.e., root mean squared error (RMSE), coefficient of determination (R^2), and mean absolute percentage error (MAPE) of all 60 cases during training and testing can be found in Supplementary Information. The results show that the R^2 varies between 0.965 and 1.000 during training and that varies between 0.912 – 1.000 during testing. For the MAPE, it varies between 0.12% and 5.96% during training while varies between 0.27% and 7.41% during testing. These metrics suggest that the accuracy of each DNN model is sufficient to characterize the effects of key parameters on battery performance despite a small portion of points with higher errors in model 8, 14, 35, etc.

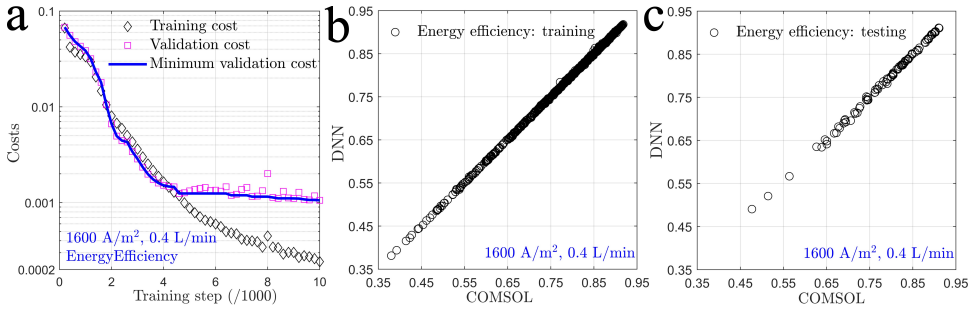

Figure 4: The evolution of the training and validation costs for one DNN (a), the 1:1 comparison between the COMSOL (ground-truth) and the predictions of a well-trained DNN during training (b) and testing (c). Testing data are independent of training data.

4.3. Sensitivity scores for energy efficiency, capacity, and energy

With the validated DNN models, sensitivity scores can be computed as mentioned in Section 2.5. Figure 5 shows the sensitivity score of energy effi-

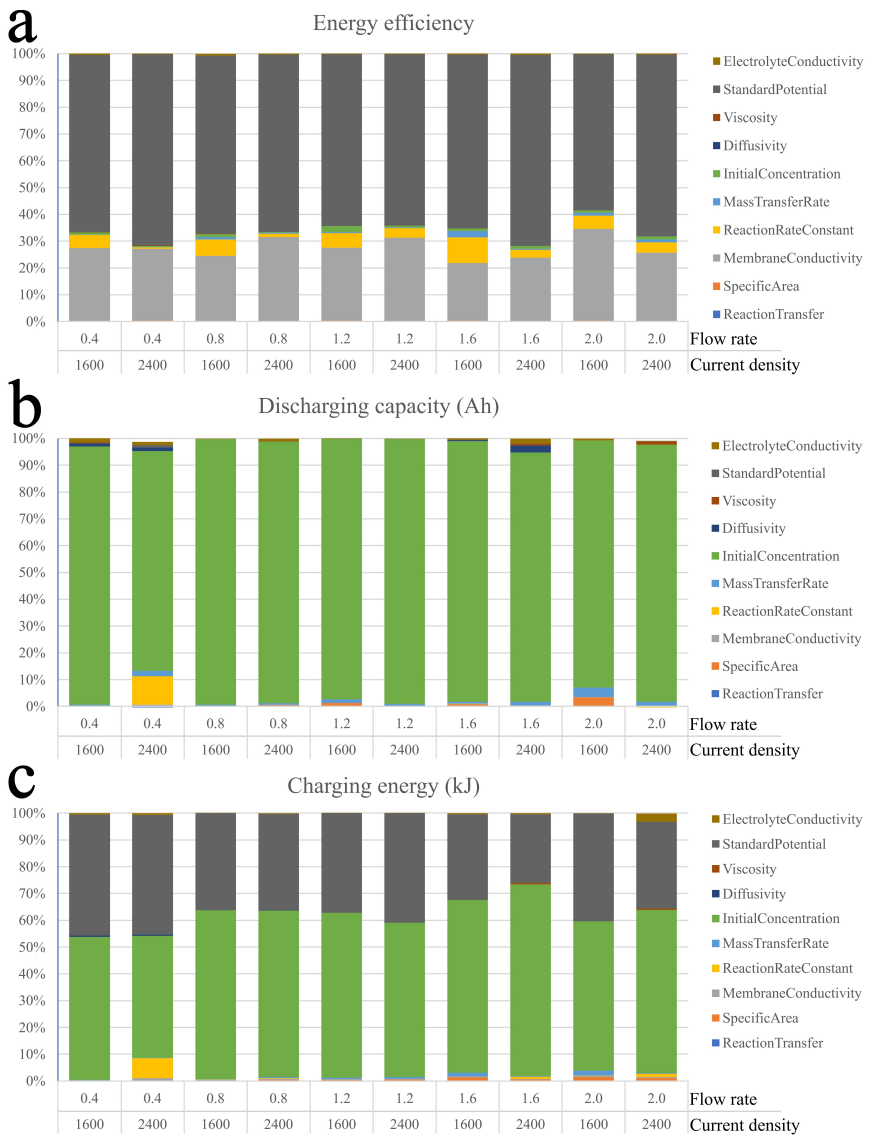

Figure 5: The sensitivity score of energy efficiency (a), discharging capacity (b), and charging energy (c) with respect to 10 physicochemical parameters at 5 flow rates and 2 current densities. Units of flow rate and current density are L/min and A/m^2, respectively.

ciency, discharge capacity, and charging energy at 5 flow rates and 2 current densities. The result shows that standard potential and membrane conduc-

tivity are the two major contributors to energy efficiency, with standard potential ranking as the most important factor controlling energy efficiency across all flow rates and current density. The reaction rate constant ranks the third for controlling the energy efficiency, while other parameters are not important. For the discharge capacity, the initial concentration of the organic active species is the dominant factor. Other parameters are not important for controlling the discharge capacity at most flow rate and current density except for the scenario with the lowest flow rate and highest current density. At the low flow rate and high current condition, the reaction rate constant contributes to around 10% of impacts on the discharging capability. For the charging energy, it is mainly controlled by the initial concentration and standard potential of the organic species with the initial concentration ranked as top control factor. Similar to the discharging capacity, the reaction rate constant contributes to around 10% impact on charging energy at lowest flow rate and highest current density. Overall, the battery performance is majorly controlled by standard potential, membrane conductivity, initial concentration across various flow rates, and current density. At very low flow rate and very high current density, the performance is also affected by the reaction rate constant in addition to the three major factors.

4.4. Dominant factors for power losses

To further evaluate the power losses, Figure 6 shows the sensitivity score of three power losses with respect to the 10 physicochemical parameters over multiple flow rates and current densities. The result shows that concentration power loss is mainly controlled by four parameters, including the electrolyte conductivity, specific area, reaction rate constant, and initial concentration,

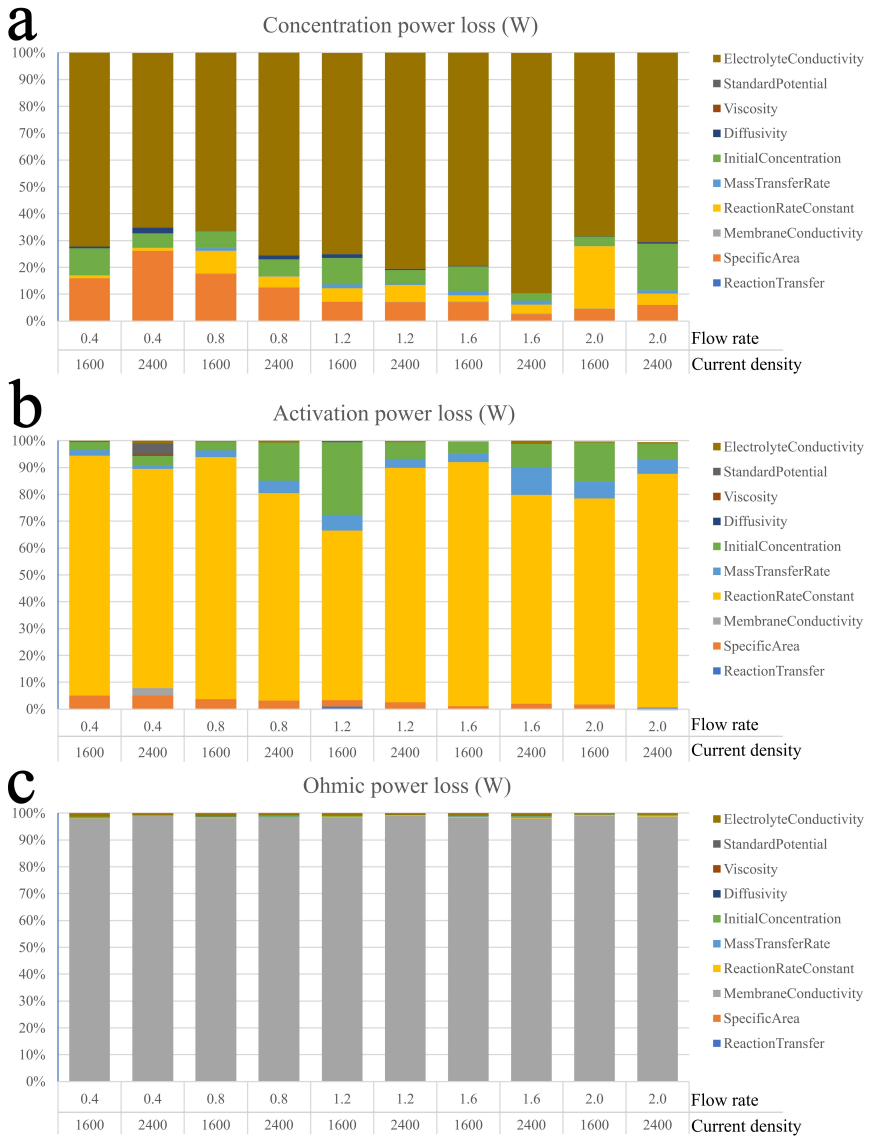

Figure 6: The sensitivity score of power losses due to concentration (a), activation (b), and ohmic (c) over-potentials.

with electrolyte conductivity ranked as the most critical factor. The dominant control factor for activation power loss is different, which is mainly

controlled by reaction rate constant and initial concentration for most of the cases. Other factors, e.g., mass transfer rate, and specific area, contribute a small portion of the activation loss. The control factor of ohmic power loss is much simpler, which is mainly controlled by membrane conductivity. Considering that ohmic power loss dominants the overall power losses, it is most critical to improve the membrane conductivity to reduce overall power losses and improve battery performance.

4.5. Sensitivity rank cross comparison

To further evaluate the impact of sensitivity quantification methodology (Step e in Figure 2), we applied the same input and output data to two additional widely used sensitivity quantification methods, i.e., MARS (Section 2.6) and SHAP (Section 2.7). The top 3 factors that control the 6 performance metrics based on the DNN, MARS, and SHAP are summarized in Table 2. The raw data used to derive such a figure can be found in the Supplementary Information. The result shows that sensitivity scores obtained from MARS are equivalent to those obtained from DNN. For the SHAP method, sensitivity scores are identical for energy efficiency, charging energy, concentration power loss, and activation power loss. However, they have minor differences in discharging capacity and ohmic power loss. Figure 7 shows the comparison of the sensitivity score of ohmic power loss derived from the three methods. It can be observed that the DNN model suggests the membrane conductivity is the only important factor, while MARS suggests both membrane conductivity and electrolyte conductivity are important, although the electrolyte conductivity has a much smaller impact. In contrast, the SHAP result suggests that the additional 5 factors, including electrolyte

Table 2: The top 3 control factors of battery performance derived from DNN, MARS, and SHAP.

Method	Performance Metrics	Standard Potential	Membrane Conductivity	Initial Concentration	Electrolyte Conductivity	Specific area & Rate Constant	Mass Transport Rate
DNN	Energy Efficiency	1	2	-	-	3	-
	Discharging Capacity	-	-	1	-	2	-
	Charging Energy	2	-	1	-	3	-
	Concentration Power Loss	-	-	3	1	2	-
	Activation Power Loss	-	-	2	-	1	-
	Ohmic Power Loss	-	1	-	-	-	-
MARS	Energy Efficiency	1	2	-	-	3	-
	Discharging Capacity	-	-	1	-	2	-
	Charging Energy	2	-	1	-	3	-
	Concentration Power Loss	-	-	3	1	2	-
	Activation Power Loss	-	-	2	-	1	-
	Ohmic Power Loss	-	1	-	-	-	-
SHAP	Energy Efficiency	1	2	-	-	3	-
	Discharging Capacity	-	-	1	-	2	3
	Charging Energy	2	-	1	-	3	-
	Concentration Power Loss	-	-	3	1	2	-
	Activation Power Loss	-	-	2	-	1	-
	Ohmic Power Loss	-	1	-	2	-	-

The 2nd and 3rd important factors are ignored when their contributions are too small compared to the most dominant factors.

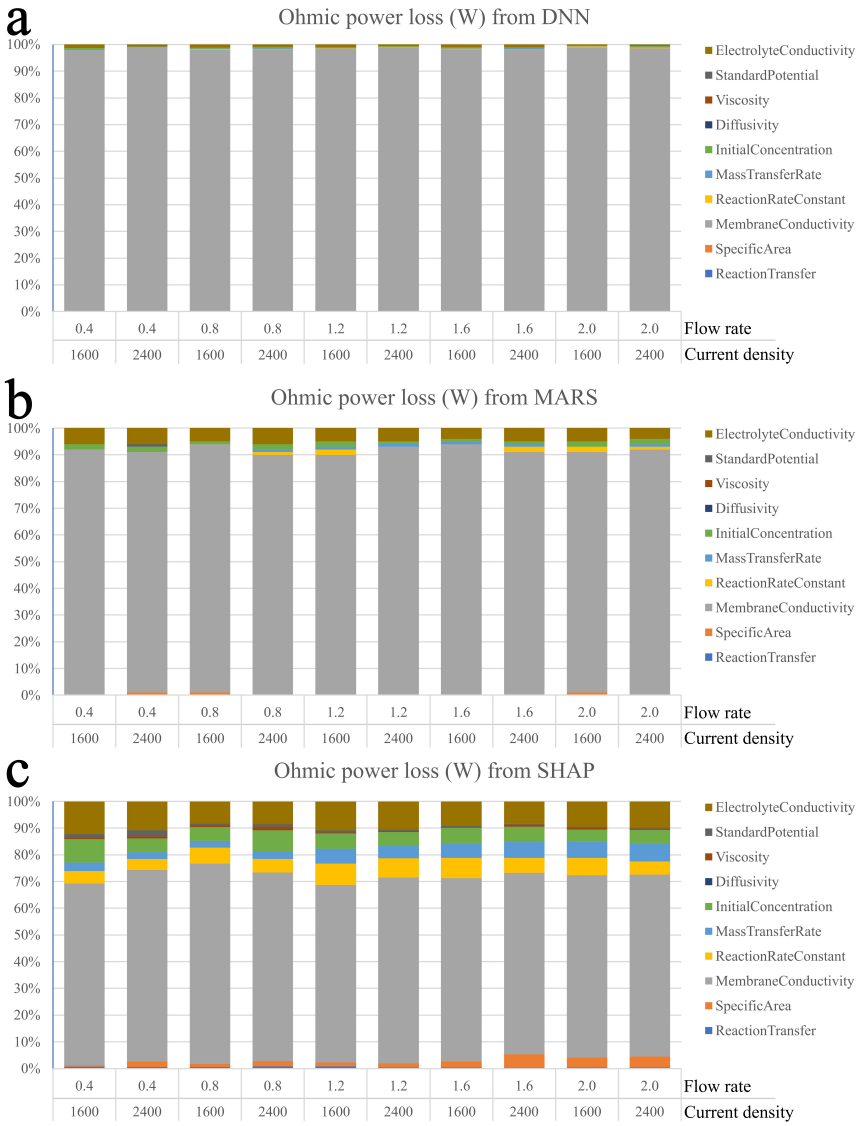

Figure 7: A comparison of the sensitivity score of ohmic power loss concerning 10 parameters from DNN, MARS, and SHAP.

conductivity, reaction rate constant, initial concentration, mass transfer rate, and specific area, together contribute to around 30% of the sensitivity score in addition to the membrane conductivity. This result suggests that all methods

are adequate to identify the most influential factors controlling the battery performance, but the SHAP can further evaluate the importance of less influential factors. These results also suggest that the flow rate and current density do not affect the relative importance of the most influential factors, but affect the quantitative accuracy, especially at high current and low flow rate scenarios.

5. Conclusions

This work demonstrated a hybrid numerical and machine learning framework for evaluating the performance of an aqueous organic redox flow battery. Specifically, a numerical model is firstly developed within COMSOL platform and validated with experiment data for both small-scale (10 cm^2) organic RFB and large-scale (780 cm^2) inorganic RFB. Following its validation, we generated 10,300 performance data with each representing the dependence of 6 performance metrics to 10 physicochemical parameters and 2 operational conditions. With these performance data, 60 DNN-based surrogate models are trained to represent the relationship between one of the 6 performance metrics and physicochemical parameters at 5 flow rates and 2 current densities. With such DNN-based surrogate models, sensitivity score of each performance metric with respect to the 10 physicochemical parameters at a given flow rate and current density can be computed and normalized to evaluate their relative importance.

Based on the sensitivity score, dominant factors that control the battery performance are identified. Specifically, the results demonstrate that 1) standard potential ranks first in controlling energy efficiency and charging

energy, 2) membrane conductivity is most critical for power loss and energy efficiency, and 3) specific area and reaction rate control activation power loss. Such discovery is not affected by the sensitivity quantification methods such as MARS and SHAP, however, less influential factors are most easily identifiable by SHAP but not DNN and MARS. This work provides a comprehensive perspective of the effects of various physicochemical parameters and operation conditions on large AORFB performance, which could guide future AORFB research and commercialization.

Acknowledgments

This research was supported by Energy Storage Materials Initiative (ESMI), which is a Laboratory Directed Research and Development Project at Pacific Northwest National Laboratory (PNNL) and U.S. Department of Energy (DOE) Office of Electricity's Rapid Operational Validation Initiative (ROVI). PNNL is a multiprogram national laboratory operated for the U.S. Department of Energy (DOE) by Battelle Memorial Institute under Contract no. DE-AC05-76RL01830.

References

[1] Amini, K., Kerr, E.F., George, T.Y., Alfaraidi, A.M., Jing, Y., Tsukamoto, T., Gordon, R.G., Aziz, M.J., 2023. An extremely stable, highly soluble monosubstituted anthraquinone for aqueous redox flow batteries. Advanced Functional Materials, 33, 2211338. doi:10.1002/adfm.202211338.

[2] Cao, J., Tao, M., Chen, H., Xu, J., Chen, Z., 2018. A highly reversible anthraquinone-based anolyte for alkaline aqueous redox flow batteries. Journal of Power Sources, 386, 40–46. doi:10.1016/j.jpowsour.2018.03.041.

[3] Chen, Y., Bao, J., Xu, Z., Gao, P., Yan, L., Kim, S., Wang, W., 2021a. A two-dimensional analytical unit cell model for redox flow battery evaluation and optimization. Journal of Power Sources, 506, 230192. doi:10.1016/j.jpowsour.2021.230192.

[4] Chen, Y., Bao, J., Xu, Z., Gao, P., Yan, L., Kim, S., Wang, W., 2023. A hybrid analytical and numerical model for cross-over and performance decay in a unit cell vanadium redox flow battery. Journal of Power Sources, 578, 233210. doi:10.1016/j.jpowsour.2023.233210.

[5] Chen, Y., Xu, Z., Wang, C., Bao, J., Koeppel, B., Yan, L., Gao, P., Wang, W., Litao, Y., Peiyuan, G., Wang, W., Yan, L., Gao, P., Wang, W., 2021b. Analytical modeling for redox flow battery design. Journal of Power Sources, 482, 228817. doi:10.1016/j.jpowsour.2020.228817.

[6] Choi, C., Kim, S., Kim, R., Choi, Y., Kim, S., Jung, H.y., Yang, J.H., Kim, H.T., 2017. A review of vanadium electrolytes for vanadium redox flow batteries. Renewable and Sustainable Energy Reviews, 69, 263–274. doi:10.1016/j.rser.2016.11.188.

[7] de la Cruz, C., Sanz, R., Suárez, A., Ventosa, E., Marcilla, R., Mavrandonakis, A., 2023. A Systematic study on the redox potentials of phenazine-derivatives in aqueous media: a combined computational and experimental work. ChemSusChem, 16, e202201984. doi:10.1002/cssc.202201984.

[8] Doetsch, C., Burfeind, J., 2022. Vanadium redox flow batteries, in: Storing Energy. Elsevier, pp. 363–381.

[9] Doetsch, C., Pohlig, A., 2020. The use of flow batteries in storing electricity for national grids, in: Future Energy. Elsevier, pp. 263–277.

[10] Feng, R., Zhang, X., Murugesan, V., Hollas, A., Chen, Y., Shao, Y., Walter, E., Wellala, N.P.N., Yan, L., Rosso, K.M., Wang, W., 2021. Reversible ketone hydrogenation and dehydrogenation for aqueous organic redox flow batteries. Science, 372, 836–840. doi:10.1126/science.abd9795.

[11] Friedman, J.H., 1991. Multivariate adaptive regression splines. The annals of statistics, 19, 1–67.

[12] Friedman, J.H., Roosen, C.B., 1995. An introduction to multivariate adaptive regression splines.

[13] Fu, Y., Bao, J., Zeng, C., Chen, Y., Xu, Z., Kim, S., Wang, W., 2023. A three-dimensional pore-scale model for redox flow battery electrode design analysis. Journal of Power Sources, 556, 232329. doi:10.1016/j.jpowsour.2022.232329.

[14] Gao, P., Yang, X., Tang, Y.H., Zheng, M., Andersen, A., Murugesan, V., Hollas, A., Wang, W., 2021. Graphical Gaussian process regression model for aqueous solvation free energy prediction of organic molecules in redox flow batteries. Phys. Chem. Chem. Phys., 23, 24892–24904. doi:10.1039/D1CP04475C.

[15] Guiheneuf, S., Godet-Bar, T., Fontmorin, J.M., Jourdin, C., Floner, D., Geneste, F., 2022. A new hydroxyanthraquinone derivative with a low and reversible capacity fading process as negolyte in alkaline aqueous redox flow batteries. Journal of Power Sources, 539, 231600. doi:10.1016/j.jpowsour.2022.231600.

[16] Hofmann, J.D., Pfanschilling, F.L., Krawczyk, N., Geigle, P., Hong, L., Schmalisch, S., Wegner, H.A., Mollenhauer, D., Janek, J., Schröder, D., 2018. Quest for Organic Active Materials for Redox Flow Batteries: 2,3-Diaza-anthraquinones and Their Electrochemical Properties. Chemistry of Materials, 30, 762–774. doi:10.1021/acs.chemmater.7b04220.

[17] Hollas, A., Wei, X., Murugesan, V., Nie, Z., Li, B., Reed, D., Liu, J., Sprenkle, V., Wang, W., 2018. A biomimetic high-capacity phenazine-based anolyte for aqueous organic redox flow batteries. Nature Energy, 3, 508–514. doi:10.1038/s41560-018-0167-3.

[18] James, G., Witten, D., Hastie, T., Tibshirani, R., Taylor, J., 2023. An Introduction to Statistical Learning. Springer Texts in Statistics, Springer International Publishing, Cham.

[19] Ji, Y., Goulet, M.A., Pollack, D.A., Kwabi, D.G., Jin, S., De Porcellinis, D., Kerr, E.F., Gordon, R.G., Aziz, M.J., 2019. A phosphonate-functionalized quinone redox flow battery at near-neutral pH with record capacity retention rate. Advanced Energy Materials, 9, 1900039. doi:10.1002/aenm.201900039.

[20] Jin, S., Jing, Y., Kwabi, D.G., Ji, Y., Tong, L., De Porcellinis, D., Goulet, M.A., Pollack, D.A., Gordon, R.G., Aziz, M.J., 2019. A water-miscible quinone flow battery with high volumetric capacity and energy density. ACS Energy Letters, 4, 1342–1348. doi:10.1021/acsenergylett.9b00739.

[21] Jing, Y., Fell, E.M., Wu, M., Jin, S., Ji, Y., Pollack, D.A., Tang, Z., Ding, D., Bahari, M., Goulet, M.A., Tsukamoto, T., Gordon, R.G., Aziz, M.J., 2022. Anthraquinone flow battery reactants with non-hydrolyzable water-solubilizing chains introduced via a generic cross-coupling method. ACS Energy Letters, 7, 226–235. doi:10.1021/acsenergylett.1c02504.

[22] Kerr, E.F., Tang, Z., George, T.Y., Jin, S., Fell, E.M., Amini, K., Jing, Y., Wu, M., Gordon, R.G., Aziz, M.J., 2023. High energy density aqueous flow battery utilizing extremely stable, branching-induced high-solubility anthraquinone near neutral pH. ACS Energy Letters, 8, 600–607. doi:10.1021/acsenergylett.2c01691.

[23] Kwabi, D.G., Lin, K., Ji, Y., Kerr, E.F., Goulet, M.A., De Porcellinis, D., Tabor, D.P., Pollack, D.A., Aspuru-Guzik, A., Gordon, R.G., Aziz, M.J., 2018a. Alkaline quinone flow battery with long lifetime at pH 12. Joule, 2, 1894–1906. doi:10.1016/j.joule.2018.07.005.

[24] Kwabi, D.G., Lin, K., Ji, Y., Kerr, E.F., Goulet, M.A., De Porcellinis, D., Tabor, D.P., Pollack, D.A., Aspuru-Guzik, A., Gordon, R.G., Aziz, M.J., 2018b. Alkaline Quinone Flow Battery with Long Lifetime at pH 12. Joule, 2, 1894–1906. doi:10.1016/j.joule.2018.07.005.

[25] Leung, P., Shah, A.A., Sanz, L., Flox, C., Morante, J.R., Xu, Q., Mohamed, M.R., Ponce de León, C., Walsh, F.C., 2017. Recent developments in organic redox flow batteries: A critical review. Journal of Power Sources, 360, 243–283. doi:10.1016/j.jpowsour.2017.05.057.

[26] Lin, K., Chen, Q., Gerhardt, M.R., Tong, L., Kim, S.B., Eisenach, L., Valle, A.W., Hardee, D., Gordon, R.G., Aziz, M.J., Marshak, M.P., 2015. Alkaline quinone flow battery. Science, 349, 1529–1532. doi:10.1126/science.aab3033.

[27] Loh, H.W., Ooi, C.P., Seoni, S., Barua, P.D., Molinari, F., Acharya, U.R., 2022. Application of explainable artificial intelligence for healthcare: A systematic review of the last decade (2011–2022). Computer Methods and Programs in Biomedicine, 226, 107161. doi:10.1016/j.cmpb.2022.107161.

[28] Pang, S., Wang, X., Wang, P., Ji, Y., 2021. Biomimetic amino acid functionalized phenazine flow batteries with long lifetime at near-neutral

pH. Angewandte Chemie International Edition, 60, 5289–5298. doi:10.1002/anie.202014610.

[29] Reed, D., Thomsen, E., Li, B., Wang, W., Nie, Z., Koeppel, B., Kizewski, J., Sprenkle, V., 2016a. Stack developments in a kW class all vanadium mixed acid redox flow battery at the Pacific Northwest National Laboratory. Journal of The Electrochemical Society, 163, A5211–A5219. doi:10.1149/2.0281601jes.

[30] Reed, D., Thomsen, E., Li, B., Wang, W., Nie, Z., Koeppel, B., Sprenkle, V., 2016b. Performance of a low cost interdigitated flow design on a 1 kW class all vanadium mixed acid redox flow battery. Journal of Power Sources, 306, 24–31. doi:10.1016/j.jpowsour.2015.11.089.

[31] Skyllas-Kazacos, M., 2022. Review—highlights of UNSW all-vanadium redox battery development: 1983 to present. Journal of The Electrochemical Society, 169, 070513. doi:10.1149/1945-7111/ac7bab.

[32] Sun, P., Liu, Y., Li, Y., Shehzad, M.A., Liu, Y., Zuo, P., Chen, Q., Yang, Z., Xu, T., 2019. 110th Anniversary: Unleashing the Full Potential of Quinones for High Performance Aqueous Organic Flow Battery. Industrial and Engineering Chemistry Research, 58, 3994–3999. doi:10.1021/acs.iecr.8b06391.

[33] Wang, C., Li, X., Yu, B., Wang, Y., Yang, Z., Wang, H., Lin, H., Ma, J., Li, G., Jin, Z., 2020. Molecular design of fused-ring phenazine derivatives for long-cycling alkaline redox flow batteries. ACS Energy Letters, 5, 411–417. doi:10.1021/acsenergylett.9b02676.

[34] Wang, C., Yang, Z., Wang, Y., Zhao, P., Yan, W., Zhu, G., Ma, L., Yu, B., Wang, L., Li, G., Liu, J., Jin, Z., 2018. High-performance alkaline organic redox flow batteries based on 2-Hydroxy-3-carboxy-1,4-naphthoquinone. ACS Energy Letters, 3, 2404–2409. doi:10.1021/acsenergylett.8b01296.

[35] Wang, C., Yang, Z., Yu, B., Wang, H., Zhang, K., Li, G., Tie, Z., Jin, Z., 2022. Alkaline soluble 1,3,5,7-tetrahydroxyanthraquinone with high reversibility as anolyte for aqueous redox flow battery. Journal of Power Sources, 524, 231001. doi:10.1016/j.jpowsour.2022.231001.

[36] Wang, C., Yu, B., Liu, Y., Wang, H., Zhang, Z., Xie, C., Li, X., Zhang, H., Jin, Z., 2021. N-alkyl-carboxylate-functionalized anthraquinone for long-cycling aqueous redox flow batteries. Energy Storage Materials, 36, 417–426. doi:10.1016/j.ensm.2021.01.019.

[37] Weber, A.Z., Mench, M.M., Meyers, J.P., Ross, P.N., Gostick, J.T., Liu, Q., 2011. Redox flow batteries: a review. Journal of Applied Electrochemistry, 41, 1137–1164. doi:10.1007/s10800-011-0348-2.

[38] Wedege, K., Dražević, E., Konya, D., Bentien, A., 2016. Organic redox species in aqueous flow batteries: redox potentials, chemical stability and solubility. Scientific Reports, 6, 39101. doi:10.1038/srep39101.

[39] Wellala, N.P.N., Hollas, A., Duanmu, K., Murugesan, V., Zhang, X., Feng, R., Shao, Y., Wang, W., 2021. Decomposition pathways and mitigation strategies for highly-stable hydroxyphenazine flow battery anolytes. J. Mater. Chem. A, 9, 21918–21928. doi:10.1039/D1TA03655F.

[40] Wu, M., Bahari, M., Jing, Y., Amini, K., Fell, E.M., George, T.Y., Gordon, R.G., Aziz, M.J., 2022. Highly stable, low redox potential quinone for aqueous flow batteries. Batteries and Supercaps, 5, e202200009. doi:10.1002/batt.202200009.

[41] Xia, X., Qin, M., Sun, Y., Shi, Y., Xu, J., Shen, Y.M., Guo, D., Chen, Z., Cao, J., 2022. A high-capacity 1,2:3,4-dibenzophenazine anode integrated into carbon felt for an aqueous organic flow battery in alkaline media. Green Chem., 24, 8783–8790. doi:10.1039/D2GC02714C.

[42] Xu, J., Pang, S., Wang, X., Wang, P., Ji, Y., 2021. Ultrastable aqueous phenazine flow batteries with high capacity operated at elevated temperatures. Joule, 5, 2437–2449. doi:10.1016/j.joule.2021.06.019.

[43] Zeng, C., Kim, S., Chen, Y., Fu, Y., Bao, J., Xu, Z., Wang, W., 2022. Characterization of electrochemical behavior for aqueous organic redox flow batteries. Journal of The Electrochemical Society, 169, 120527. doi:10.1149/1945-7111/acadad.

[44] Zeng, C., Kim, S., Chen, Y., Fu, Y., Bao, J., Xu, Z., Wang, W., 2023. In situ characterization of kinetics, mass transfer, and active electrode surface area for vanadium redox flow batteries. Journal of The Electrochemical Society, 170, 030507. doi:10.1149/1945-7111/acbf7f.

[45] Zhang, C., Yuan, Z., Li, X., 2024. Designing better flow batteries: an overview on fifty years' research. ACS Energy Letters, 9, 3456–3473. doi:10.1021/acsenergylett.4c00773.